

Defect Engineering in Ce-Doped Aluminum Garnet Single Crystal Scintillators

Martin Nikl,^{*,†} Kei Kamada,[‡] Vladimir Babin,[†] Jan Pejchal,^{†,‡} Katerina Pilarova,[§] Eva Mihokova,[†] Alena Beitlerova,[†] Karol Bartosiewicz,[†] Shunsuke Kurosawa,^{‡,||} and Akira Yoshikawa^{‡,||}

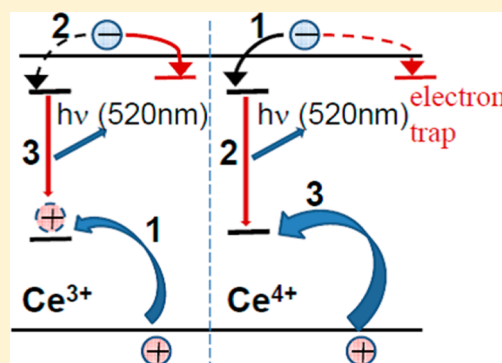
[†]Institute of Physics AS CR, Cukrovarnicka 10, 16253 Prague, Czech Republic

[‡]New Industry Creation Hatchery Center (NICHe), Tohoku University, 6-6-10 Aoba, Aramaki, Aoba-ku, Sendai, Miyagi, Japan

[§]Faculty of Nuclear Sciences and Physical Engineering, Czech Technical University in Prague, Brehova 7, 115 19 Prague, Czech Republic

^{||}Institute for Materials Research, Tohoku University, 2-1-1 Katahira, Aoba-ku, Sendai, 980-8577 Japan

ABSTRACT: Mg-codoped $\text{Lu}_3\text{Al}_5\text{O}_{12}:\text{Ce}$ single crystal scintillators were prepared by a micropulling down method in a wide concentration range from 0 to 3000 ppm of Mg codopant. Their structure and chemical composition were checked by X-ray diffraction and electron probe microanalysis techniques. Absorption and luminescence spectra, photoluminescence decays, and thermoluminescence glow curves were measured together with several other scintillation characteristics, namely, the scintillation decay, light yield, afterglow, and radiation damage to reveal the effect of Mg codoping. Several material characteristics manifest a beneficial effect of Mg codoping. We propose a model explaining the mechanism of material improvement which is based on the stabilization of a part of the cerium dopant in the tetravalent charge state. The stable Ce^{4+} center provides an additional fast radiative recombination pathway in the scintillation mechanism and efficiently competes with electron traps in garnet scintillators.



1. INTRODUCTION

Cerium-doped aluminum garnet single crystals of the chemical formula $\text{Ln}_3\text{Al}_5\text{O}_{12}$, $\text{Ln} = \text{Y}, \text{Lu}$ (LnAG) are well-known scintillators where the former was widely applied a time ago in the cathodoluminescent detectors in electron microscopy,¹ and the latter has undergone an intense research and development in the past decade, see the review in ref 2, the result of which is material with a density of 6.67 g/cm³, light yield exceeding 25000 phot/MeV, energy resolution at 662 keV approaching 5%, and scintillation response dominated by 50 ns decay time.^{2–4} Yet, the light yield of LuAG:Ce single crystals is well below the theoretical limit of about 60 000 phot/MeV,⁵ and the reason for that are shallow electron traps associated with the Lu_{Al} antisite defects in the melt-grown crystals.⁶ Recent discovery of so-called multicomponent garnets, prepared by the balanced admixture of Gd and Ga cations into the LuAG (YAG) structure, established a new material group with a strongly enhanced light yield up to more than 50 000 phot/MeV.^{2,7,8} Such high values are achieved due to burying the mentioned electron traps into the conduction band whose bottom is decreasing.⁹ However, simultaneous decrease of ionization barrier between the relaxed 5d^1 excited state of Ce^{3+} and the bottom of the conduction band disables an application of these materials at higher temperatures due to the excited state ionization problem.^{10–12}

Recent studies of the Ce^{3+} -doped Lu_2SiO_5 (LSO) and $(\text{Lu},\text{Y})_2\text{SiO}_5$ (LYSO) scintillators have shown that Me^{2+} codoping ($\text{Me} = \text{Ca}, \text{Mg}$) does play a positive role in their performance,¹³ and the effect was explained as due to creation of the stable Ce^{4+} center. This center forms a new fast radiative recombination pathway based on the immediate electron capture from the conduction band, radiative de-excitation of the excited Ce^{3+} center, and a hole capture to return to the Ce^{4+} stable initial state.^{14,15} Such a mechanism works in parallel with the standard one based on the stable Ce^{3+} center. This somewhat unexpected result found its analogue in the Ca-codoped YAG:Ce.¹⁶ This earlier overlooked study shows the same Ce^{3+} emission band in the cathodoluminescence spectrum, even in the case in which the Ce^{3+} absorption bands were completely wiped out by Ca^{2+} codoping; i.e., all cerium ions were converted into the stable tetravalent state. Very recently, such an approach has been used in Mg-codoped LuAG:Ce scintillation ceramics whose light yield was enormously enhanced, and the presence of Ce^{4+} was clearly identified by its characteristic charge transfer (CT) absorption in the near UV range below 350 nm.¹⁷ In fact, very similar values of the onset of this CT absorption process in the above-

Received: July 4, 2014

Revised: July 28, 2014

Published: July 30, 2014

mentioned orthosilicate (identified already in 1994¹⁸) and aluminum garnet structures, see Figure 1, provide a strong support for such interpretation.

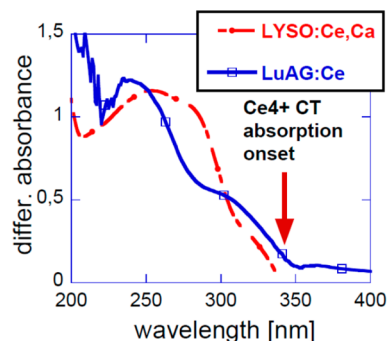


Figure 1. Ce⁴⁺-related induced absorption in Ce-doped LYSO and LuAG single crystals; the data are taken from refs 17 and 19.

As reported in this paper, we studied the effect of Mg codoping in a broad concentration range in LuAG:Ce single crystals grown from the melt by the micropulling down (μ -PD) technique. In the melt-grown aluminum garnet crystals, such a strategy is of paramount importance as the Ce⁴⁺ center can compete for an immediate electron capture from the conduction band with the above-mentioned shallow and any other electron traps. This competition enhances the fastest part of the scintillation response at the expense of unwanted slow components. We show that Mg-codoping leads to enormous improvement of several scintillation characteristics of LuAG:Ce while keeping its stable scintillation efficiency up to high temperatures.

2. EXPERIMENTAL DETAILS

2.1. Crystal Growth Procedure. A stoichiometric mixture of 4 N Mg₂CO₃, CeO₂, Lu₂O₃, and α -Al₂O₃ powders (High Purity Chemicals Co.) was used as the starting material. Nominally, starting powders were prepared according to the formula (Mg_x, Ce_y, Lu_{1-y})₃Al₅O₁₂(CO)_{x/2}. Single crystals of LuAG:Ce,Mg were grown by the μ -PD method with a radio frequency heating system. The value for y was 0.002 and x was 0, 0.0001, 0.0005, and 0.003. These samples will be designated as Mg-0, 100, 500, 3000 from now on. A schematic draft of the μ -PD growth apparatus is given in ref 20. Typical pulling rates were 0.05–0.07 mm/min, and the diameter was around 3 mm. Crystals were grown from an Ir crucible under the N₂ atmosphere. The seed crystals were $\langle 111 \rangle$ oriented undoped LuAG crystals. Plates of $\phi 3$ mm \times 1 mm were cut and polished for the absorption and luminescence spectra measurements, while the rest of the rods was used for the structure and chemical composition analyses.

A commercial high quality LuAG:Ce single crystal grown by the Czochralski method from 5 N raw materials, under reducing atmosphere from molybdenum crucible in CRYTUR, Czech Republic, was used for comparisons, and in the following text it is designated as LuAG:Ce-Cz. Furthermore, Bi₄Ge₃O₁₂ (BGO) single crystal of a high quality (light yield (LY) \approx 8500 phot/MeV) is used for quantitative comparisons of both the scintillation efficiency and afterglow.

2.2. Characterization of Obtained Phase. Pieces of the grown crystals were crushed and ground into powders in a mortar. Powder X-ray diffraction analysis was carried out in the 2θ range 15–75° using the RINT Ultima (RIGAKU) diffractometer. The CuK α X-ray source was used, and the accelerating voltage and current were 40 kV and 40 mA, respectively.

Quantitative chemical analyses of the crystals for the Ce, Lu, and Al content along the radius and growth direction were performed by the electron probe microanalysis (EPMA; JXA-8621MX, JEOL). So called ZAF correction is used, where Z , A , and F are the atomic number,

absorption correction factor, and fluorescence correction factor, respectively. X-ray fluorescence analysis (XRF) was also performed to determine chemical composition of grown crystals by Rigaku ZSX primus II.

2.3. Absorption and Luminescence Characteristics. Absorption spectra were measured by the Shimadzu 3101PC spectrometer in the 190–1200 nm range. At the custom-made 5000M model fluorometer Horiba Jobin Yvon equipped with the photon counting detector TBX-04 (IBH Scotland) the radioluminescence (RL) spectra and fast photoluminescence decays of Ce³⁺ were measured under an X-ray (40 kV, 10 mA) tube (Seifert GmbH) and the nanoLED 450 nm excitation sources, respectively. Janis cryostat (77–800 K) was used to the measure temperature dependence of photoluminescence decays. Thermoluminescence (TSL) measurements in the 30–600 °C temperature range were performed by Harshaw Model 3500 Manual TLD Reader with a heating rate of 1 °C/s. Samples were irradiated at RT with the ⁶⁰Co source and received a dose of 0.8 Gy.

2.4. Light Yield and Scintillation Decay Measurements. Light yield measurements were carried out using a Hybrid photomultiplier (HPMT) under ¹³⁷Cs (662 keV) radioisotope excitation. Pulse height spectra were measured using the setup with HPMT DEP PP0470 and by spectroscopic amplifier ORTEC 672 with the shaping time of 1 μ s with accuracy $\pm 5\%$. Light yield (LY) values were calculated from those of photoelectron yield employing integral quantum efficiency of the used HPMT, and wavelengths of emission spectra of crystals. The used HPMT PP0470 photomultiplier has the highest quantum efficiency $\sim 25\%$ in the UV spectral range 200–400 nm, while in the visible spectral range 450–600 nm its quantum efficiency decreases from 20 to 7%. On the basis of emission spectra, the calculated integral quantum efficiency for LuAG:Ce is about 9%. Scintillation decay curves were obtained by using the Hamamatsu PMT U7600 and digital oscilloscope TDS3052 under excitation by 662 keV photons from ¹³⁷Cs.

3. RESULTS AND DISCUSSION

Mg 0, 100, 500, 3000 ppm codoped Ce1%:LuAG crystals were grown by the μ -PD method. A photograph of the set is shown in Figure 2. The grown crystals were transparent with a yellow

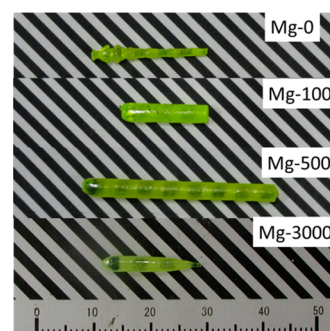


Figure 2. Photograph of the grown Mg-codoped LuAG:Ce single crystals.

color and 2–3 mm in diameter and 20–40 mm in length. Some of them look slightly cloudy because of the rough surface coming from the thermal etching. The Mg-3000 sample rod shows a visibly less yellowish appearance. The inner part of all the crystals is perfectly transparent.

Powder X-ray diffraction was performed to identify the crystal phase of grown crystals. The results of the powder X-ray diffraction of the grown Mg 0, 100, 500, 3000 ppm codoped Ce1%:LuAG crystals are shown in Figure 3. All of the grown crystals show the single cubic garnet phase.

The Ce distribution of 3000 ppm codoped Ce1%:LuAG in a radial direction is shown in Figure 4a. An increase of the dopant

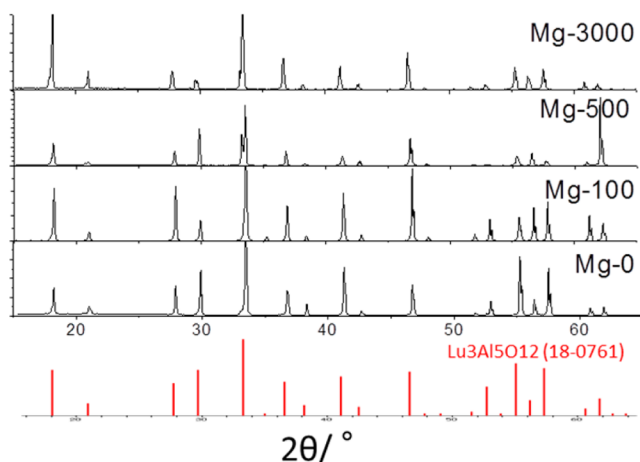


Figure 3. Results of the powder X-ray diffraction of the Mg 0, 100, 500, 3000 ppm codoped Ce1%:LuAG crystals.

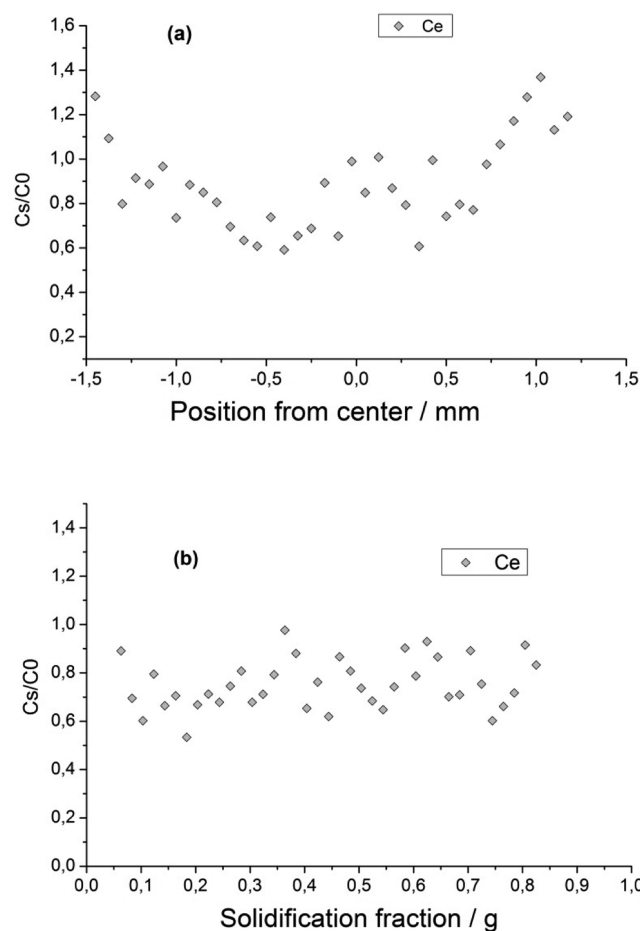


Figure 4. Ce distribution along the radius (a) and growth direction (b) of the 3000 ppm codoped Ce1%:LuAG crystal. C_s and C_0 are concentrations in the crystal and starting material, respectively.

toward the outer region of the sample is observed, which is typical in situation where the dopant radius is comparatively bigger compared to the cation site.⁷ The composition distribution along the growth direction of 3000 ppm codoped Ce1%:LuAG is shown in Figure 4b. According to the previous report,⁷ the effective segregation coefficients of Ce were $k_{\text{eff}} < 1$, considering the diagnostic distribution curves. The effective

segregation coefficient of Ce ions in LuAG host shows values of $k_{\text{eff}} = 0.697$, which is the value of about 10 times higher compared to LuAG:Ce(Pr) crystal growth by the Czochralski method.² Mg concentration in the crystals was not detected either by EPMA or XRF due to the high detection limit of XRF (100 wt ppm).

The absorption spectra of the sample set are presented in Figure 5 together with that of the standard LuAG:Ce-Cz

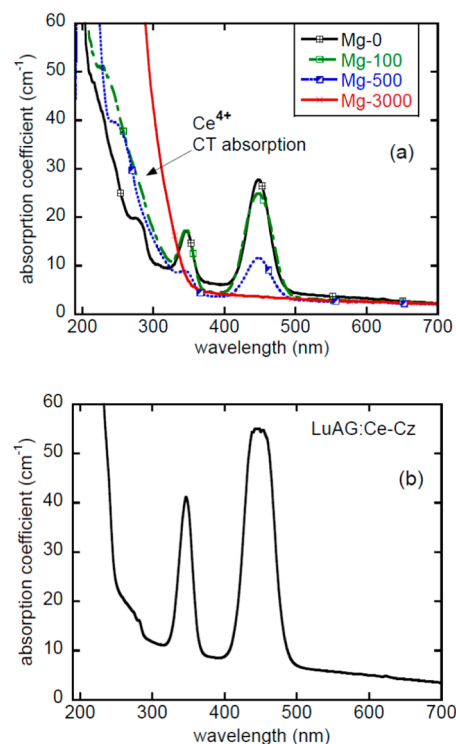


Figure 5. Absorption spectra of the Mg-codoped LuAG:Ce sample set grown by micropulling down method (a) and of LuAG:Ce standard sample (b).

crystal. In the latter sample, the amplitude of 4f-5d¹ absorption band at 445 nm is somewhat saturated in Figure 5b due to reaching the experimental limit of the spectrometer and/or parasitic contribution of Ce³⁺ luminescence to the signal beam. Consequently, the ratio of 445 nm/347 nm absorption band amplitudes is perturbed by this experimental artifact. With increasing concentration of Mg codopant, the Ce⁴⁺ CT absorption is clearly enhanced while the intensity of the Ce³⁺ 4f-5d¹ absorption band decreased. The latter absorption band is completely wiped out for the highest Mg concentration 3000 ppm.

Radioluminescence (RL) spectra were measured with carefully defined conditions to ensure mutual comparison of emission intensities in an absolute scale among all the samples. RL spectra in Figure 6 show an abrupt enhancement of the Ce³⁺ emission band between the Mg-0 and Mg-100 samples. With the further increasing Mg concentration, its intensity smoothly decreases and for Mg-3000 is comparable with the Mg-0 sample. Variable shape and intensity of UV emission are related to the host properties. Absolute intensity in the Mg-100 sample is comparatively higher with respect to the standard crystal. The Mg-500 sample was accidentally contaminated by Gd³⁺ impurity in the process of the sample preparation.

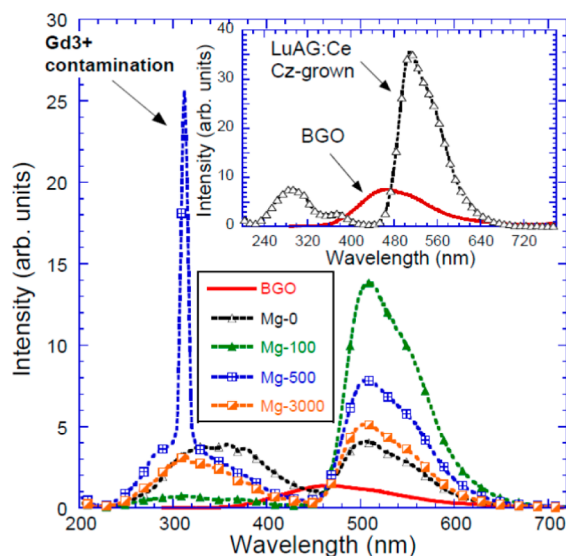


Figure 6. Radioluminescence spectra of the Mg-codoped LuAG:Ce sample set and that of the standard crystal (in the inset). Excitation X-ray tube, 40 kV, 15 mA. The spectra are mutually comparable in an absolute scale.

In the Mg-100 sample, the temperature dependence of photoluminescence decay time of Ce^{3+} center was measured, see Figure 7, to find the onset of thermal quenching and/or

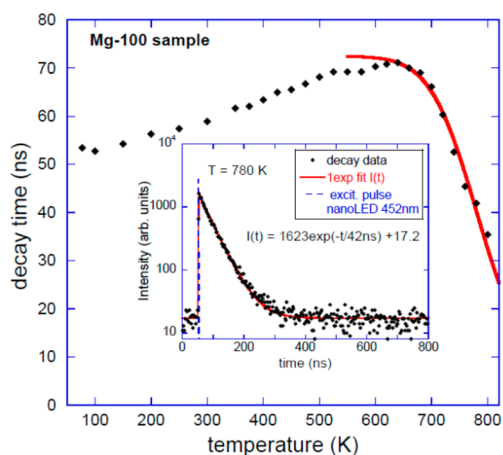


Figure 7. Temperature dependence of photoluminescence decay times for Mg-100 sample obtained from a single exponential approximation; see an example of the decay and its approximation by a function $I(t)$ in the inset for $T = 780$ K. Excitation by nanoLED 452 nm, emission wavelength set at 520 nm. Solid line is the approximation obtained by eq 1 described in the text.

thermal ionization process which puts the upper temperature limit for the scintillator use. In multicomponent garnets, such an onset varies depending on the content of Gd and Ga cations within 50–150 °C approximately.^{10–12} For a YAG:Ce0.033% powder, it was reported around 600–650 K and became progressively lowered with an increase of Ce concentration due to concentration quenching.²¹ In the present case, the onset of the decay time shortening is around 700 K. A simple equation for the decay time temperature dependence is used to fit experimental data

$$1/\tau_{\text{obs}}(T) = 1/\tau_{\text{rad}} + w_0 \times \exp(-\Delta E/kT) \quad (1)$$

where τ_{obs} and τ_{rad} are the observed at temperature T and radiative decay times, respectively. Parameters w_0 and ΔE describe the quenching pathway being the frequency factor and energy barrier, respectively, and their values are calculated as $1.37 \times 10^7 \text{ s}^{-1}$ and 1.15 eV, respectively; see the result given by the solid line in Figure 7. A smooth increase of decay time with temperature within 100–600 K was found in several Ce-doped luminescence materials and ascribed to temperature dependence of the transition dipole moment.²² However, due to partial overlap of the absorption and emission spectra of Ce^{3+} , see Figures 5 and 6, which will certainly increase with temperature due to bands broadening, the self-absorption and radiation trapping effect is probable, also resulting in the decay time increase.²³

Scintillation light yield values are collected in Table 1. One can see a similar trend as in RL spectra in Figure 6 with a very high value for the Mg-100 sample exceeding by 34% that of the standard LuAG:Ce-Cz crystal. Scintillation decays for Mg-0 and standard LuAG:Ce-Cz crystal show a typical two component decay curve⁶ based on the prompt and delayed radiative recombination at the Ce^{3+} centers. The latter, slow component extending over several orders of magnitude in the time scale, down to tens of microseconds,²⁴ becomes gradually reduced with increasing Mg content and wiped out for the Mg-3000 sample; see also Figure 8.

Another application-important characteristics is the scintillation afterglow, a critical parameter, e.g., in CT imaging. A reduction of the signal at least 3 orders of magnitude in several ms after the X-ray cutoff is required for a good contrast imaging without memory effects. Such traps can also decrease scintillation efficiency and/or cause its instabilities, which has been recently well demonstrated in the study of “bright burn” effects in scintillation materials.^{25,26} In Figure 9, the afterglow curves of this kind are provided for the entire sample set together with BGO which is known by its extremely low afterglow.²⁷ The relative values of afterglow intensity at 4 ms and at 400 ms after X-ray cutoff (the signal level with X-rays being on is normalized to 1), are reported in Table 1. It is

Table 1. Survey of Light Yield Values (Excitation ^{22}Na , 511 keV, Shaping Time 1 μs), Scintillation Decay Constants (Excited by ^{137}Cs , 662 keV), Afterglow (Excitation X-ray, 40 kV) and Induced Absorption Characteristics (Irradiation X-ray, 40 kV, 15 mA, 30 min)

sample	light yield (ph/MeV)	T1(ns)/ I1(%)	T2(ns)/ I2(%)	afterglow at 4 ms(%) / 400 ms(%)	ind abs coefficient at 510 nm (cm^{-1})
Mg-0	4850	58/48	300/52	19/8.3	2.1
Mg-100	23100	48/58	380/42	1.3/0.08	n.m.
Mg-500 ^a	18800	48/57	275/43	2.5/0.07	n.m.
Mg-3000	14100	15/11	51/89	0.2/0.03	0.004
LuAG-Ce-Cz	17200	58/42	958/58	2.9/0.4	<0.002

^aThe values of light yield and afterglow can be slightly negatively affected by slow parasitic Gd^{3+} emission line at 312 nm; see Figure 6.

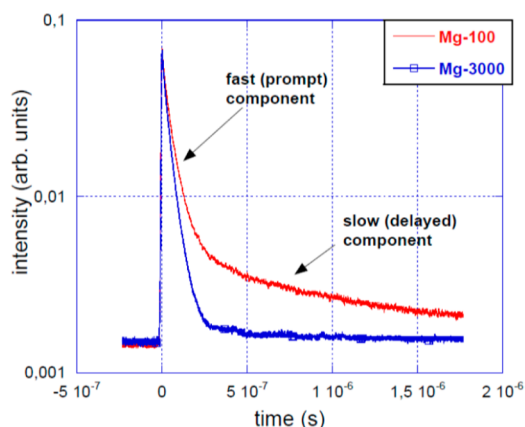


Figure 8. Spectrally unresolved scintillation decays of Mg-100 and Mg-3000 samples. Excitation ^{137}Cs , 667 keV.

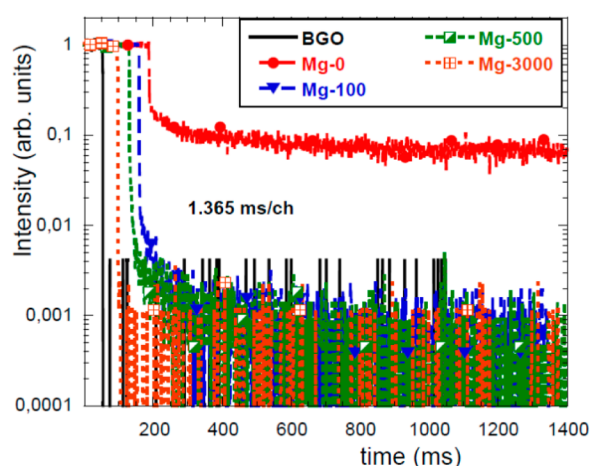


Figure 9. Normalized, spectrally unresolved afterglow of Mg-0, 100, 500, and 3000 together with that of BGO standard sample. Visually higher level of afterglow signal in few channels of BGO afterglow is due to the counting detection technique and lower intensity of BGO scintillation before the X-ray cutoff.

worth noting that all Mg-codoped crystals show lower afterglow intensities compared to the standard LuAG:Ce-Cz crystal. An ultralow signal level, approaching that of the BGO standard sample, was measured in the Mg-3000 sample.

Finally, the radiation resistance of the sample set was tested under an X-ray irradiation (40 kV, 15 mA, 30 min, estimated dose 300 Gy) by the measurement of the induced absorption IA (λ) evaluated from the equation

$$\text{IA}(\lambda) = \{A_{\text{irr}}(\lambda) - A_0(\lambda)\} \times 2.3/d \text{ (cm)} \quad (2)$$

where $A_{\text{irr}}(\lambda)$ and $A_0(\lambda)$ are absorbance values after and before X-ray irradiation, respectively and d (cm) is the sample thickness. The $A_{\text{irr}}(\lambda)$ and $A_0(\lambda)$ spectra are shown in Figure 10 for Mg-0 and Mg-3000 samples. The latter sample, compared to the former, shows an extremely low value of the induced absorption at the emission peak at 510 nm; see Table 1.

It is difficult to speculate about the nature of the induced absorption bands in these samples with the experimental data available. Most probably, the Mg^{2+} itself will not create any energy levels in the forbidden gap of LuAG as the forbidden gap of MgO is 7.8 eV,²⁸ about 0.5 eV broader compared to that of LuAG,²⁹ and the top of valence band will be at similar

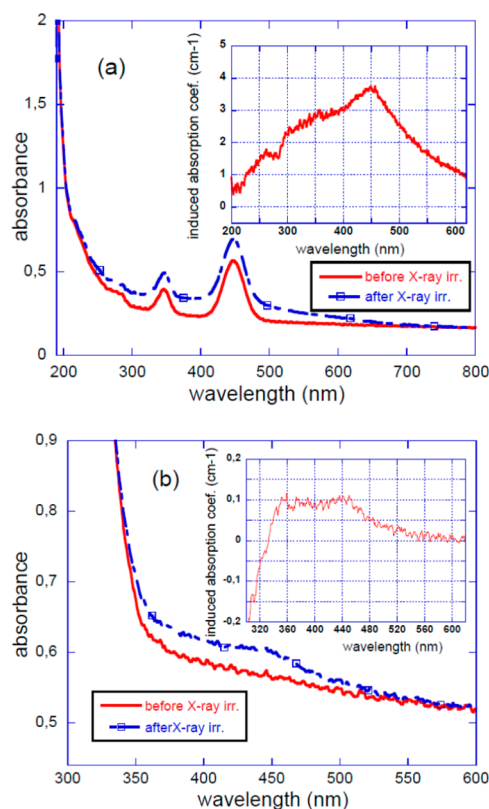


Figure 10. $A_{\text{irr}}(\lambda)$ and $A_0(\lambda)$ spectra are shown for the Mg-0 (a) and Mg-3000 (b) samples with the calculated induced absorption IA (λ) spectra in the inset. Irradiation by X-ray, 40 kV, 10 mA, 30 min, estimated dose 300 Gy.

absolute levels determined by the oxygen 2p wave functions in both MgO and LuAG compounds. The Mg^{2+} doping, however, would induce the hole O-centers due to charge compensation in the undoped LuAG, and such hole centers might show broad absorption bands throughout UV and visible spectral regions based on the radiation induced absorption spectra of aluminum garnets.³⁰ Consequently, this aspect appears quite complex and requires a separate investigation.

The set of Mg-codoped samples was also characterized by a spectrally unresolved TSL glow curve measurement, Figure 11.

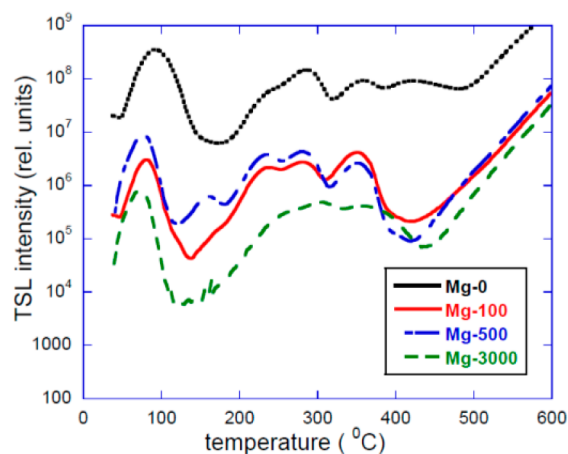


Figure 11. TSL glow curves of the set of Mg-codoped LuAG:Ce samples. Irradiation at RT was performed by ^{60}Co radioisotope, dose 0.8 Gy.

All the samples show TSL maxima at similar temperatures of about 45, 80–90, 160, 230, 280, and 350 °C, and the positions of most of them are similar to those reported before for the Czochralski grown LuAG:Ce.³¹ The rapid signal increase above 450 °C is due to blackbody radiation. However, there is an evident trend in decreasing glow curve intensity with increasing Mg concentration when the samples are compared: the integrals of the glow curves are in the ratio 1:8.2:5.6:374 for the Mg-3000, Mg-500, Mg-100, and Mg-0 samples, respectively. TSL glow curve integral and light yield values are well correlated with the observed increase in the radiation hardness when the Mg-0 and Mg-3000 samples are compared. The decrease of TSL glow curve intensity over the entire range of temperatures with increasing Mg concentration appears advantageous in comparison with Ca-codoping applied in multicomponent garnet $\text{Gd}_3\text{Ga}_3\text{Al}_3\text{O}_{12}\text{:Ce}$ single crystal scintillator recently.³² The latter codoping induced a deep trap related to an intense TSL glow curve peak at 390 K. Significant light yield decrease occurred as well.

On the basis of the above-reported characteristics and effects of Mg-codoping in LuAG:Ce, one can distinguish two Mg concentration intervals of practical interest. The first one, within 100–500 ppm, appears promising in obtaining a noticeably higher light yield and scintillation response with somewhat suppressed slower component as well as afterglow intensity, when compared to a very good quality commercial Czochralski grown LuAG:Ce sample. Such material can be useful for medical imaging or elsewhere.

The reason for such an improvement can be explained with the help of Figure 12, where the sequence of steps in scintillation mechanism is sketched for the stable Ce^{3+} (left part) and Ce^{4+} (right part) centers:

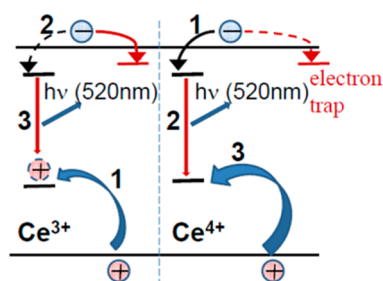


Figure 12. Sketch of the scintillation mechanism at the stable Ce^{3+} (left) and Ce^{4+} (right) emission centers.

In step no. 1, in the first picoseconds of scintillation mechanism, the Ce^{4+} center can efficiently compete with any electron traps (due to antisite defects, oxygen vacancies) for an immediate capture of electrons from conduction band. The stable Ce^{3+} center is much less effective in such competition as it first needs to capture the hole from the valence band in step no. 1.

In step no. 2 the Ce^{4+} , transformed into an excited Ce^{3+} center, emits the desired scintillation photon, i.e., contributes to the fastest part of scintillation response. In the same step the Ce^{3+} center, converted into temporary Ce^{4+} , captures an electron from conduction band and becomes excited.

In step no. 3 the return into the initial state (beginning of cycle) is accomplished by the hole capture from the valence band (Ce^{4+} in the right part) and by emission of scintillation photon (Ce^{3+} in the left part).

It is worth mentioning that the last step in the Ce^{4+} scintillation mechanism (right part), the hole capture from valence band, must always be nonradiative, i.e., not contributing to an afterglow. Though the source of such delayed holes is not clear at this moment, the shallow hole traps have been shown at low temperature TSL measurements in an undoped LuAG,⁶ and their occurrence might be even spatially correlated with the divalent codopant, i.e., with Ce^{4+} centers themselves.¹⁷

The second Mg concentration interval involves concentrations around 3000 ppm. The Mg concentration of 3000 ppm already completely wiped out the stable Ce^{3+} centers; i.e., practically all cerium ions were converted into the tetravalent charge state. In this sample, compared to the commercial LuAG:Ce-Cz standard, the light yield is only by 18% lower, but its scintillation response lacks any slower component, and its fast part is yet noticeably accelerated; see Figure 8. Most importantly, compared to the commercial LuAG:Ce-Cz standard, its afterglow is more than 1 order of magnitude lower due to the nonradiative character of last step in its scintillation mechanism sketched in Figure 12. Considering also its excellent radiation hardness and suppressed reabsorption effects due to lacking 4f-5d¹ absorption band of Ce^{3+} , such a material can be promising for future inorganic fiber-based calorimeter detectors at high energy physics accelerators where LuAG:Ce is one of the best candidate materials.³³

Another important advantage of the studied Mg-codoped LuAG:Ce scintillators is their high temperature stability. It is derived from the temperature dependence of photoluminescence decay times of Ce^{3+} center which show the onset of thermal quenching/thermal ionization of the 5d¹ excited state around 700 K; see Figure 7. Temperature stability of Ce^{3+} center in LuAG host is similar to that found in YAG:Ce,²¹ and to our best knowledge it is the highest among fast heavy scintillators based on 5d-4f luminescence of Ce^{3+} , Pr^{3+} , or Nd^{3+} emission centers.

Finally, we mention that among various attempts to codope the Ce- or Pr-doped aluminum garnets by Zr^{4+} ,³¹ Hf^{4+} and Yb^{2+34} or Si^{4+35} in the case of single crystals and simultaneous using of sintering aids based on Si^{4+} and Mg^{2+} in the case of LuAG:Pr optical ceramics³⁶ the overall change of optical and scintillation characteristics did not point to any practically important improvement, while in the case of Mg^{2+} codoping in LuAG:Ce reported in this work truly dramatic improvement in several scintillation parameters has been achieved.

4. CONCLUSIONS

The Mg-codoped LuAG:Ce single crystals were manufactured by the micropulling down method, and their optical, luminescence, and scintillation characteristics were measured and compared with the Czochralski grown commercial LuAG:Ce single crystal and BGO single crystal as well.

The Mg-codoping has shown several highly beneficial effects on LuAG:Ce scintillator. For low concentrations in the range 100–500 ppm, the light yield is strongly enhanced, and even in this early stage of development it significantly exceeds that of the Czochralski grown commercial sample. Furthermore, the scintillation decay and afterglow parameters are also more favorable in the Mg-codoped crystals in this concentration range. For high Mg concentration of 3000 ppm, the light yield is only by 18% inferior to that of Czochralski grown crystal, but the scintillation response lacks any slow components; afterglow is improved by another 1–2 orders of magnitude and approaches the characteristics of BGO, which is considered

one of the best existing materials regarding the afterglow intensity. In addition, radiation hardness monitored through the induced absorption after X-ray irradiation increased enormously. Such materials, after being adapted to the Czochralski growth and optimized with respect to Mg concentration in low and high ranges, have a great application potential in fast imaging and high energy physics, respectively. Moreover, due to very high temperature stability of Ce^{3+} centers evidenced from the photoluminescence decay time measurement, such materials can be also used in high temperature applications up to 430 °C at least.

Favorable effects of Mg^{2+} codoping are explained by the creation of the stable Ce^{4+} centers in the LuAG structure. Such centers create another fast radiative recombination pathway working in parallel with the classical mechanism based on the stable Ce^{3+} centers. Such optimization strategy can be used also in other scintillation materials whenever the Ce^{3+} scintillation spectrum does not overlap with the charge transfer absorption of Ce^{4+} centers.

AUTHOR INFORMATION

Corresponding Author

*Phone: +420220318445; fax: +420 233343184; e-mail: nikl@fzu.cz.

Notes

The authors declare no competing financial interest.

ACKNOWLEDGMENTS

Czech MEYS KONTAKT LH14266 and Czech Science foundation 13-09876S projects, Crystal Clear Collaboration in CERN, and EC Marie Curie Initial Training Network LUMINET, no. 316906 are gratefully acknowledged. Health Labour Sciences Research Grant, The Japanese Ministry of Health Labour Development of Systems and Technology for Advanced Measurement and Analysis (SENTAN), Japan Science and Technology Agency (JST), adaptable and Seamless Technology Transfer Program through Target-driven R&D (A-STEP), JST are also acknowledged for support.

REFERENCES

- (1) Autrata, R.; Schauer, P.; Kvapil, J.; Kvapil, J. *J. Phys. E* **1978**, *11*, 707–708.
- (2) Nikl, M.; Yoshikawa, A.; Kamada, K.; Nejezchleb, K.; Stanek, C. R.; Mares, J. A.; Blazek, K. *Prog. Cryst. Growth Charact. Mater.* **2013**, *59*, 47–72.
- (3) Dujardin, C.; Mancini, C.; Amans, D.; Ledoux, G.; Abler, D.; Auffray, E.; Lecoq, P.; Perrodin, D.; Petrosyan, A.; Ovanessian, K. L. *J. Appl. Phys.* **2010**, *108*, 013510.
- (4) Mares, J. A.; Nikl, M.; Beitlerova, A.; Horodysky, P.; Blazek, K.; Bartos, K.; D'Ambrosio, C. *IEEE Trans. Nucl. Sci.* **2012**, *59*, 2120–2125.
- (5) Dorenbos, P. *IEEE Trans. Nucl. Sci.* **2010**, *57*, 1162–1167.
- (6) Nikl, M.; Vedda, A.; Fasoli, M.; Fontana, L.; Laguta, V. V.; Mihokova, E.; Pejchal, J.; Rosa, J.; Nejezchleb, K. *Phys. Rev. B* **2007**, *76*, 195121.
- (7) Kamada, K.; Yanagida, T.; Endo, T.; Tsutsumi, K.; Fujimoto, Y.; Fukabori, A.; Yoshikawa, A.; Pejchal, J.; Nikl, M. *Cryst. Growth Des.* **2011**, *11*, 4484–4490.
- (8) Kamada, K.; Yanagida, T.; Endo, T.; Tsutsumi, K.; Usuki, Y.; Nikl, M.; Fujimoto, Y.; Fukabori, A.; Yoshikawa, A. *J. Cryst. Growth* **2012**, *352*, 88–90.
- (9) Fasoli, M.; Vedda, A.; Nikl, M.; Jiang, C.; Uberuaga, B. P.; Andersson, D. A.; McClellan, K. J.; Stanek, C. R. *Phys. Rev. B* **2011**, *84*, 081102(R).
- (10) Ogieglo, J. M.; Katelnikovas, A.; Zych, A.; Jüstel, T.; Meijerink, A.; Ronda, C. R. *J. Phys. Chem. A* **2013**, *117*, 2479–2484.
- (11) Ueda, J.; Aishima, K.; Tanabe, S. *Opt. Mater.* **2013**, *35*, 1952–1957.
- (12) Luo, J.; Wu, Y.; Zhang, G.; Zhang, H.; Ren, G. *Opt. Mater.* **2013**, *36*, 476–481.
- (13) Spurrier, M. A.; Szupryczynski, P.; Yang, K.; Carey, A. A.; Melcher, C. L. *IEEE Trans. Nucl. Sci.* **2008**, *55*, 1178–1182.
- (14) Blahuta, S.; Bessiere, A.; Viana, B.; Dorenbos, P.; Ouspenski, V. *IEEE Trans. Nucl. Sci.* **2013**, *60*, 3134–3141.
- (15) Kärner, T.; Laguta, V. V.; Nikl, M.; Shalapska, T.; Zazubovich, S. *J. Phys. D: Appl. Phys.* **2014**, *47*, 065303.
- (16) Rotman, S. R.; Tuller, H. L.; Warde, C. J. *Appl. Phys.* **1992**, *71*, 1209–1214.
- (17) Liu, S.; Feng, X.; Zhou, Z.; Nikl, M.; Shi, Y.; Pan, Y. *Phys. Status Solidi RRL* **2014**, *8*, 105–109.
- (18) Visser, R.; Melcher, C. L.; Schweizer, J. S.; Suzuki, H.; Tombrello, T. A. *IEEE Trans. Nucl. Sci.* **1994**, *41*, 689–693.
- (19) Chewpraditkul, W.; Wanarak, C.; Szczesniak, T.; Moszynski, M.; Jary, V.; Beitlerova, A.; Nikl, M. *Opt. Mater.* **2013**, *35*, 1679–1684.
- (20) Yoshikawa, A.; Epelbaum, B. M.; Hasegawa, K.; et al. *J. Cryst. Growth* **1999**, *205*, 305–316.
- (21) Bachmann, V.; Ronda, C.; Meijerink, A. *Chem. Mater.* **2009**, *21*, 2077–2084.
- (22) Lyu, L.-J.; Hamilton, D. S. *J. Lumin.* **1991**, *48&49*, 251–254.
- (23) Auzel, F.; Bonfigli, F.; Gagliari, S.; Baldacchini, G. *J. Lumin.* **2001**, *94&95*, 293–297.
- (24) Chewpraditkul, W.; Swiderski, L.; Moszynski, M.; Szczesniak, T.; Syntfeld-Kazuch, A.; Wanarak, C.; Limsuwan, P. *IEEE Trans. Nucl. Sci.* **2009**, *56*, 3800–3805.
- (25) Dell'Orto, E.; Fasoli, M.; Ren, G.; Vedda, A. *J. Phys. Chem. C* **2013**, *117*, 20201–20208.
- (26) Moretti, F.; Patton, G.; Belsky, A.; Fasoli, M.; Vedda, A.; Trevisani, M.; Bettinelli, M.; Dujardin, C. *J. Phys. Chem. C* **2014**, *118*, 9670–9676.
- (27) Gevay, G. *Prog. Cryst. Growth Charact.* **1987**, *15*, 145–186.
- (28) Whited, R. C.; Flaten, C. J.; Walker, W. C. *Solid State Commun.* **1973**, *13*, 1903–1905.
- (29) Babin, V.; Blazek, K.; Krasnikov, A.; Nejezchleb, K.; Nikl, M.; Savikhina, T.; Zazubovich, S. *Phys. Status Solidi C* **2005**, *2*, 97–100.
- (30) Nikl, M.; Mihokova, E.; Laguta, V.; Pejchal, J.; Baccaro, S.; Vedda, A. *SPIE* **2007**, *6586*, 65860E.
- (31) Vedda, A.; Di Martino, D.; Martini, M.; Laguta, V. V.; Nikl, M.; Mihokova, E.; Rosa, J.; Nejezchleb, K.; Blazek, K. *Phys. Status Solidi A* **2003**, *195*, R1–R3.
- (32) Tyagi, M.; Meng, F.; Koschan, M.; Donald, S. B.; Rothfuss, H.; Melcher, C. L. *J. Phys. D: Appl. Phys.* **2013**, *46*, 475302.
- (33) Lecoq, P. *J. Phys. Conf. Ser.* **2009**, *160*, 012016.
- (34) Derdzian, M. V.; Ovanessian, K. L.; Petrosyan, A. G.; Belsky, A.; Dujardin, C.; Pedrini, C.; Auffray, E.; Lecoq, P.; Lucchini, M.; Pauwels, K. *J. Cryst. Growth* **2012**, *361*, 212–216.
- (35) Baccaro, S.; Cecilia, A.; Mihokova, E.; Nikl, M.; Nejezchleb, K.; Blazek, K. *IEEE Trans. Nucl. Sci.* **2005**, *52*, 1105–1108.
- (36) Shen, Y.; Feng, X.; Shi, Y.; Vedda, A.; Moretti, F.; Hu, C.; Liu, S.; Pan, Y.; Kou, H.; Wu, L. *Ceram. Int.* **2014**, *40*, 3715–3719.